Eur. Phys. J. Special Topics **222**, 3071–3087 (2013)

DOI: 10.1140/epjst/e2013-02076-9

THE EUROPEAN
PHYSICAL JOURNAL
SPECIAL TOPICS

Review

Colloidal particles at fluid interfaces: Effective interactions, dynamics and a gravitation–like instability

J. Bleibel[1,2], A. Domínguez[3], and M. Oettel[1,a]

[1] Institut für Angewandte Physik, Universität Tübingen, Auf der Morgenstelle 10, 72076 Tübingen, Germany
[2] Max-Planck-Institut für intelligente Systeme, Heisenbergstr. 3, 70569 Stuttgart, Germany
[3] Física Teórica, Universidad de Sevilla, Apdo. 1065, 41080 Sevilla, Spain

Received 6 September 2013 / Received in final form 17 September 2013

Abstract. Colloidal particles of micrometer size usually become irreversibly trapped at fluid interfaces if they are partially wetted by one phase. This opens the chance to create two–dimensional model systems where the effective interactions between the particles are possibly influenced by the presence of the interface to a great extent. We will review recent developments in the quantitive understanding of these effective interactions with a special emphasis on electrostatics and capillarity. Charged colloids of micrometer size at an interface form effective dipoles whose strength sensitively depends on the double layer structure. We discuss the success of modified Poisson–Boltzmann equations with regard to measured colloidal dipole moments. On the other hand, for somewhat larger particles capillary interactions arise which are long–ranged and analogous to two–dimensional screened Newtonian gravity with the capillary length λ as the screening length. For colloidal diameters of around 10 micrometer, the collective effect of these long–ranged capillary interactions will dominate thermal motion and residual, short–ranged repulsions, and results in an instability towards a collapsed state for a finite patch of particles. Such long–ranged interactions with the associated instability are also of interest in other branches of physics, such as self-gravitating fluids in cosmology, two–dimensional vortex flow in hydrodynamics, and bacterial chemotaxis in biology. Starting from the colloidal case we develop and discuss a dynamical "phase diagram" in the temperature and interaction range variables which appears to be of more general scope and applicable also to other systems.

1 Introduction

Knowledge of the effective interactions between colloids in solutions is an issue of great practical importance. Also for basic research it is a problem of significant

---

[a] e-mail: martin.oettel@uni-tuebingen.de

interest because the study of these effective interactions requires the whole arsenal of classical and statistical physics due to the possible richness of colloidal interactions. Nowadays the design of effective tailored interactions is possible or within reach and systems with such tailored interactions are interesting from the more fundamental point of view of providing tunable many–body systems which allow explicit tests on mesoscopic scales of numerous predictions of statistical physics.

During the last twenty years, there has been an increasing interest in investigating colloids trapped at fluid interfaces. Since partially wetting colloids are trapped almost irreversibly at fluid interfaces, these colloids form an effectively two–dimensional (2D) system. Since structural properties of condensed matter sensitively depend on the spatial dimension d, one can expect that these model systems provide access to new phenomena not occurring in bulk systems. The presence of a deformable interface is expected to modify the effective interactions between the colloids qualitatively, in that interface–mediated interactions (capillary interactions) may arise which have no counterpart in the bulk, and quantitatively because the known solvent–mediated bulk interactions will also change due to the simultaneous presence of two different solvents forming the interface.

In many experimental systems, charged colloids are trapped at an interface between an electrolyte (water plus ions) and a low–ϵ dielectric such as air or oil. The charges lead to repulsive electrostatic interactions, and for spherical colloids these dominate the effective interactions when the colloids radius is $\lesssim 1\,\mu$m. By now they can be measured rather precisely [1–5]. In Sect. 2.1 we discuss the electrostatics at an electrolyte interface with special regard to the implications for modification strategies for the Poisson–Boltzmann equation. For general colloidal shape, capillary interactions can be attractive, repulsive, or both in the case of orientational anisotropy. Here we concentrate on the research of the past five years. Earlier work has been reviewed in Refs. [6–9]. A particular focus will be on systems where the capillary interaction will be long–ranged and attractive and dominates all other interactions (Sect. 2.2). Here, an instability arises similar to a gravitational instability of two–dimensional matter subject to gravitational attraction. Owing to this instability, the dynamics of such systems is particularly interesting (Sect. 3).

2 Effective interactions at interfaces

2.1 Partially charged colloids at interfaces: Electrostatic interactions

Whenever a charged surface is immersed in a thermal solvent with mobile co– and counterions (usually an aqueous electrolyte), a screening layer of counterions will form in the vicinity of the charged surface, giving rise to the so called "double layer". Very often surfaces can be highly charged (e.g. colloid surfaces attain charge densities of about one elementary charge e per nm^2) such that the electrostatic potential ψ near the surface exceeds the equivalent of the thermal energy $k_\mathrm{B}T = 1/\beta$ by far (for room temperature $k_\mathrm{B}T/e$ corresponds to a potential of 25 mV). Thus the arrangements of water molecules and counterions near and at the surface should display fairly strong correlations, resulting in e.g. nontrivial potential and dielectric profiles. For charged particles at the interface between an electrolyte and a nonpolar medium (air, oil with dielectric constant $\epsilon_\mathrm{np} \lesssim 2\epsilon_0$, ϵ_0 is the dielectric constant of vacuum) the surface charges can only reside on the colloid surface exposed to the electrolyte. (See, however, Ref. [5] regarding some evidence for residual charges on the oil side.) The double layer screens the colloid charge only to the extent that no monopole field is present along the interface. However, higher multipole fields are present, and the leading multipole is a dipole with moment p_z oriented perpendicular to the interface (regardless of the charge distribution on the colloid [10]). Consequently, the electrostatic interaction energy between two charged colloids at the interface with mutual distance d is long–ranged and $\propto p_z^2/d^3$. If the local curvature at the colloid surface is smaller than the inverse Debye–Hückel screening length κ then the double layer can be approximated by the double layer of a charged wall in the vicinity of each point at the colloid–electrolyte interface. The dipole moment $p_z = A^{\mathrm{eff}} p'_{\mathrm{wall}}$ can be calculated from the areal dipole moment density p'_{wall} and an effective area A^{eff} which depends on the precise colloid geometry. The crucial observation is that $p'_{\mathrm{wall}} = \epsilon_0 \psi_{\mathrm{wall}}$ is proportional to the contact potential at the wall.[1] Thus the interaction energy at *large distances* between two colloids is proportional to the *square of the wall contact potential.* Since the wall contact potential is sensitive to the details of the double layer structure, we have a colloidal probe for the double layer using these large–distance interactions at the interface. This is drastically different from the situation in a bulk electrolyte: there the large distance interaction energy between two charged colloids depends only on the two renormalized charges on the colloids. These in turn saturate with increasing charge density on the colloids, thus they contain no information about the double layer close to the colloid surfaces.

The simplest double layer model (neglecting ion correlations) is derived from the Poisson–Boltzmann equation,

$$\boldsymbol{\nabla} \cdot (\epsilon \boldsymbol{\nabla} \psi) = 2 c_s e \sinh(\beta e \psi). \tag{1}$$

Here, c_s is the bulk number density of positive/negative ions in the solvent. For an electrolyte with $\epsilon = \mathrm{const.}$, $\kappa^{-1} = (\epsilon/(2c_s\beta e^2))^{1/2}$, and the dimensionless potential $\phi = \beta e \psi$. Using, these quantities, the Poisson–Boltzmann equation becomes $\boldsymbol{\nabla} \cdot \boldsymbol{\nabla}\phi = \kappa^2 \sinh\phi$, and the significance of the screening length becomes immediately obvious in its linearized form, $(\boldsymbol{\nabla} \cdot \boldsymbol{\nabla} - \kappa^2)\phi = 0$, which entails an exponentially decaying potential with characteristic length κ^{-1} around a localized charge distribution.

The Poisson–Boltzmann solution for a charged wall with (high) charge density σ_c gives a reduced dipole moment of $\beta e p'_{\mathrm{wall}} \approx 2\epsilon_0 \ln(\beta e/(\kappa\epsilon)\ \sigma_c)$. Thus one sees that the wall dipole moment (and consequently also the colloid dipole moment p_z) will not saturate with increasing charge density on the colloid and depends logarithmically on both screening length and charge density. A full numerical solution with the proper geometry of a spherical colloid trapped at an interface (with arbitrary contact angle) has confirmed the simple "wall model" for the effective collloid dipole strength p_z [11]. Also, the Poisson–Boltzmann equation predicts qualitatively correctly the different change in contact angle for positively vs. negatively charged colloids, due to the finite surface potential of the electrolyte interface [12].

Experiments. – The dipole moment can be calculated from the interaction potential between charged colloids and this can be inferred through laser tweezers on isolated pairs of colloids, from inversion of measured pair correlations or from elasticity measurements on 2D crystals at the interface. Whereas the logarithmic dependence on κ^{-1} has received much support from laser tweezer data [1], the absolute magnitude of p_z from the Poisson–Boltzmann equation is too small by about a factor of 5 compared to results of careful measurements using all three routes [2]. This points to a severe underestimation of the contact potential at a charged wall in the Poisson–Boltzmann equation.

---

[1] Let the wall be located at $z = 0$ and the double layer be located in the half–space $z > 0$. Then $p'_{\mathrm{wall}} = \int_{0+}^{\infty} (z\rho(z) + P(z))dz$ where $\rho(z)$ is the charge density in the double layer and $P(z) = -(\epsilon(z) - \epsilon_0)\partial_z\psi(z)$ is the polarization density of the solvent. Since $\partial_z(\epsilon\partial_z\psi) = \rho$, we have $p'_{\mathrm{wall}} = \int_{0+}^{\infty} \epsilon_0 \partial_z \psi = \epsilon_0 \psi_{\mathrm{wall}}$.

Modification strategies for improving the Poisson–Boltzmann description. – Modifications of the Poisson–Boltzmann equation while retaining its local character have been of long–standing interest in the soft–matter and physico–chemical communities. Since the interface experiments of Ref. [2] provide data for the colloid dipole moment and thus also for the contact potential, it is interesting to check whether modifications of the Poisson–Boltzmann equation are able to reproduce these values. The following physical mechanisms can be incorporated into modified Poisson–Boltzmann equations:

1. Finite size effects. – A finite size of the co– and counterions (e.g. through a hard–sphere volume v) will inevitably lead to layering effects in the density profile of the ions near the charged surface. In aqueous solution, the effective ion size is increased as a result of hydration. Thus, in a strict sense, the finite ion size contributions require nonlocal treatment, however, one can capture these effects using local corrections, for example, by taking into account a local change in the ion chemical potential. A popular modification (MPB, modified Poisson–Boltzmann equation) [13] has been derived by lattice gas considerations. Applied to the double layer, one finds that the screening behavior far from the concentrated region is not qualitatively changed, but rather the effective position of a charged surface is shifted into the solution. Although the lattice gas modification corresponds to a not very precise equation of state for hard spheres, application of MPB to inhomogeneous ionic solution yields predictions that compare rather well with exact results. This points to some internal cancellation of errors.
2. Dielectric inhomogeneity of the solvent. – The solvent medium, made up of water molecules with permanent dipoles, acts as a dielectric which is polarized in an external electrostatic field and thus screens the electrostatic potential within the medium. Thermal fluctuations favor isotropic orientation of dipoles, and the electrostatic interactions favor alignment with the field lines. As long as the thermal energy exceeds the electrostatic counterpart, the polarization is proportional to an external field and the dielectric constant is field independent. But if the two energy scales become comparable, polarization saturation takes place: the dipoles reach perfect alignment with the field lines and no longer dissipate electrostatic energy above a certain threshold. This behavior can be described through an electric–field dependent dielectric “constant” (see e.g. the dipolar Poisson–Boltzmann equation of [14] and the Langevin Poisson–Boltzmann equation of [15]).
3. Ionic polarizabilities. – Ions can further be characterized by including their polarizability α, so that they acquire an induced dipole moment in an external field. Part of the electrostatic energy is dissipated when it polarizes ions. This leads again to a modification of the dielectric “constant” with a term linear in the ion concentration, $\epsilon_{\text{eff}} \to \epsilon + \alpha(c_+ + c_-)$, see e.g. [16,17].
4. Stern layer. – A layer of solvent in direct contact with an interface has different properties from the bulk solvent. First, ions cannot penetrate into it due to their finite size. Second, the solvent within this layer tends to be more structured so that its dielectric response is expected to be suppressed in relation to that in the bulk. A frequent solution to incorporating this contribution is to introduce the Stern layer adjacent to a sharp interface with the width corresponding to a radius of a bare or hydrated ion and the dielectric constant the same as or lower than the bulk value.

According to the results of Ref. [15], a finite ion size, dielectric saturation and the incorporation of the Stern layer lead to a noticeable increase in the contact potential which is in line with the experimental results (discussed above) for the dipole moment

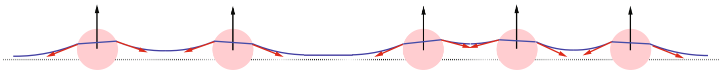

Fig. 1. The interfacial deformation induces a force on each particle applied at the corresponding contact line. The projection onto the reference plane is the effective capillary interaction between the particles. The vertical projection balances possible vertical forces acting on the particle, e.g., the weight.

of charged colloids at interfaces. Inclusion of ionic polarizabilities [16] decreases the contact potential, but the effect is small for realistic ionic polarizabilities. However, a match of the experimental data can only be achieved at the expense of strong variation of ion concentrations and of the solvent dielectric response within less than a nanometer. This clearly points to the necessity of going beyond local modifications of the Poisson–Boltzmann equation [18,19]. Potentially, precise measurements of the colloidal dipole moment at an interface for different types of salt und varying salt concentration can give valuable constraints on further model building.

2.2 Capillary interactions

In the previous subsection, we considered the electrostatic interactions at a *flat* interface which is justifiable for small particles (see also Ref. [20]). The particles trapped at the fluid interface will deform it in general, leading to an effective interaction between the particles of capillary origin. The theoretical framework to describe this effective force has been reviewed recently in Refs. [9,21]. We present here the key ideas and results.

The deformation of the interface is determined by the Young–Laplace equation, while the effect of a particle shows up both in the boundary conditions (at the particle–interface contact line) as in the pressure discontinuity entering the Young–Laplace equation. This effect will depend on physicochemical properties of the particle, such as shape, contact angle, electrical charge, or the force acting on the particle. It is physically realistic to assume small deformations out of a reference, flat interface if the particles are not too close to each other (typical deformations lie in the nanometer range when the particle separation is in the micrometer range). As a consequence, the Young–Laplace equation can be linearized and the interfacial deformation can be written formally as a multipolar expansion with multipole coefficients depending on intrinsic particle properties ("permanent capillary multipole") or also on the environment ("induced capillary multipole") [9]. The small deformation creates a net pull in the plane of the reference interface located at the contact line, see Fig. 1, leading to a capillary interaction between the particles in the effective 2D system forming the monolayer. This interaction can be likewise written as a multipolar expansion, so that the problem of effective capillary interaction is actually transformed into the problem of computing the (permanent as well as induced) multipoles. It can be shown that the capillary monopole and dipole are given respectively as the vertical force (with respect to the reference flat interface) of the force acting on the particle other than capillary, and the component of the torque in the reference plane [22]. Higher order capillary multipoles are related to the shape of the particle.

The dominant term at large separations is the interaction between permanent monopoles, given as

$$V_{\mathrm{cap}}(d) = -\frac{f^2}{2\pi\gamma} K_0\left(\frac{d}{\lambda}\right) . \tag{2}$$

Here, K_0 denotes a modified Bessel function, λ is the *capillary length*, γ is the surface tension of the interface, and f is the strength of the capillary monopole.

The potential $V_{\mathrm{cap}}(d)$ describes an attraction with a range of the order of λ, because $V_{\mathrm{cap}}(d \gg \lambda) \sim \exp(-d/\lambda)$. In the opposite limit, $V_{\mathrm{cap}}(d \ll \lambda) \sim \ln d$, which is formally identical to 2D Newtonian gravity. Actually, the parallelism with gravity is deeper because $\lambda \sim$ mm typically while the interparticle separation $d \sim \mu$m at most for colloidal monolayers, so that a single particle is interacting simultaneously with a large number of neighbours $N \sim (\lambda/d)^2$, via a non-integrable potential. In this sense, the capillary attractions can be termed "long–ranged", and all other forces between the particles (hard core, electric repulsion,...) will be called "short–ranged".

The range and strength of the interaction described by Eq. (2) is easily controllable in experimental setups: either through the value of the parameters γ or λ or through the strength of the capillary monopole f. The latter can be due to the weight of the particle or to another external field, e.g., an electrostatic field, as described in Refs. [23–25]. In this manner the monopolar capillary force can be tuned to become the dominant interaction in the system.

In the absence of external force and torque, the capillary interaction is dominated at large separations by the force between permanent quadrupoles. They arise naturally as soon as the particles are non spherical. As a consequence, the interaction is anisotropic, the relative orientation of the particles is an additional relevant degree of freedom, and the corresponding capillary interaction can be either attractive or repulsive. Numerous experimental works have studied the quadrupolar capillary force recently, see, e.g., [26–31] and the review in Ref. [32].

In certain circumstances, the capillary interaction can be dominated asymptotically by *induced* capillary multipoles. This is the case when the far–field interfacial deformation is dominated by the electric field due to charged particles (see [9] and Refs. therein). More recently, this has also been shown to be the case at a fluid–nematic interface when the deformation is dominated by the elastic stresses induced by the particle in the nematic phase [33]. Nevertheless, in both cases the ensuing effective capillary interaction is subdominant compared to the interparticle force due to the electric charges or the elastic stresses, respectively.

As has been illustrated, the multipolar expansion is particularly useful for the determination of the interaction asymptotically at larger separations. At separations comparable to the particle radius, all multipolar terms are roughly comparable and the mathematically more involved, full problem "Young–Laplace equation + position of the contact line + boundary conditions at the contact line" has to be solved, which is amenable only to numerical evaluation. See, e.g., Ref. [34] for a recent example.

Finally, we remark that the multipole expansion is also useful to address the capillary force that the particles experience due to a *prescribed* curvature of the interface created by, e.g., boundary conditions on the border of the interface. Provided the curvature radius is much larger than the interparticle separation, one can take the tangent plane as the reference plane and study the coupling of the capillary multipoles with the prescribed small deformation away from the reference plane [9,22]. See Refs. [22,35–37] for the case of a capillary monopole trapped at a spherical interface, and Refs. [9,22,38,39] for the analysis of the induced quadrupole on a curved interface. References [29,30] present experimental studies of a permanent quadrupole trapped in a curved interface.

3 Dynamics and the gravitation-like instability

3.1 Capillary–driven dynamics

There are not many works dealing with the dynamical evolution driven by capillary interactions and most of them have concentrated specifically on the motion of one or two particles under the effect of the quadrupolar capillary force, see, e.g., Refs. [29,30] for recent works. As an exception one can cite Ref. [40] for the experimental study of the collective collapse under capillary attraction, or Refs. [41–43] for studies how particles are trapped by the fluid interface.

In Ref. [44] a model was introduced to describe the *collective* dynamics, modelled by an evolution equation for the 2D particle number density, $\varrho(\mathbf{r}, t)$, at the monolayer, $\mathbf{r} = (x, y)$, driven by monopole–monopole capillary attraction, see Equation (2). It was based on three simplifying assumptions:

1. *Local equilibrium*: The characteristic time scales of evolution are sufficiently large so that the forces can be described by a local equilibrium ansatz. Furthermore, for the short–ranged forces the force per unit area is approximated as $(\nabla = (\partial_x, \partial_y))$
$$\mathbf{F}_{\text{short}}(\mathbf{r}, t) \approx -\nabla p(\varrho = \varrho(\mathbf{r}, t)), \tag{3}$$
expressed in terms of the equilibrium equation of state for the pressure, $p(\varrho)$, of the 2D fluid in the absence of capillary deformations, assuming isothermal conditions. The temperature is a constant parameter fixed by the upper and lower fluids acting as thermal baths, and thus it is irrelevant for the temporal evolution. Equation (3) is a local approximation, restricting the validity of the model to density fields smooth over the microscopic length scales.
2. *Mean field*: The capillary force is computed assuming that the interfacial deformation is small and adjusts instantaneously to the momentary particle distribution, i.e., it satisfies the Young–Laplace equation for a given particle distribution $\varrho(\mathbf{r}, t)$. Furthermore, a mean–field approximation is used so that the capillary force per unit area can be expressed as
$$\mathbf{F}_{\text{cap}} = f \varrho \nabla U, \tag{4}$$
with the ensemble averaged mean–field interfacial deformation $U(\mathbf{r})$, determined self–consistently by the mean–field Young–Laplace equation:
$$\nabla^2 U - \frac{U}{\lambda^2} = -\frac{f}{\gamma} \varrho. \tag{5}$$
The mean–field approximation is justified by the long range of the capillary interaction and enters in the neglect of correlations between the position of the particles experiencing the capillary force (expressed by the local density ϱ in Eq. (4)) and the position of the particles inducing the interfacial deformation (local density ϱ in Eq. (5)). The pair potential in Eq. (2) can be expressed as $V_{\text{cap}}(d) = -f U_\delta(d)$ in terms of Green's function $U_\delta(d)$ of Eq. (5), i.e., the solution for a single–particle source $\varrho(\mathbf{r}) = \delta(\mathbf{r})$.
3. *Overdamped motion*: Inertia of the particles is neglected, so that the in-plane velocity field $\mathbf{v}(\mathbf{r}, t)$ of the 2D particle distribution is proportional to the driving force,
$$\varrho \mathbf{v}(\mathbf{r}, t) = \Gamma(\mathbf{F}_{\text{short}} + \mathbf{F}_{\text{cap}}), \tag{6}$$
where Γ is the effective single–particle mobility at the interface. For reasons of simplicity the effect of hydrodynamic interactions is neglected in Eq. (6), and Γ is taken to be constant in space and time.

Under these conditions, mass conservation leads to the following form of the continuity equation:
$$\frac{\partial \varrho}{\partial t} = -\nabla \cdot (\varrho \mathbf{v}) = \Gamma \nabla \cdot (\nabla p - f \varrho \nabla U). \tag{7}$$

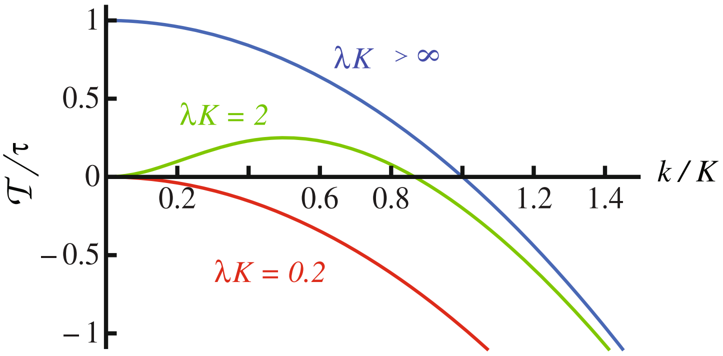

Fig. 2. Plot of the inverse characteristic time given by Eq. (9) for three qualitatively different cases. (Figure taken from Ref. [44].)

Together with Eq. (5), this set of equations describe the competition between clustering driven by the capillary attraction and the homogenization tendency caused by the short–ranged forces. The evolution described by this set of equations has been studied using theoretical approaches, numerical solutions and N–body simulations [44–46]. The findings can be summarized as follows:

- *Linear stability of an infinitely extended homogeneous distribution* [44,45]: a sinusoidal perturbation, $\varrho(\mathbf{r},0) = C\varrho_0 \exp(-i\mathbf{k}\cdot\mathbf{r})$, of the initially homogeneous distribution ϱ_0 evolves in time to lowest order in $|C| \ll 1$ as

  $$\varrho(\mathbf{r},t) = C\varrho_0 \exp(-i\mathbf{k}\cdot\mathbf{r} + t/\tau(k)), \tag{8}$$

  according to Eqs. (5,7). The characteristic inverse time,

  $$\frac{1}{\tau(k)} = \mathcal{T}^{-1}\left[\frac{1}{1+(\lambda k)^{-2}} - \left(\frac{k}{K}\right)^2\right], \tag{9}$$

  depends on the wave number and is given in terms of the so-called *Jeans' time and wave number*, respectively,

  $$\mathcal{T} = \frac{\gamma}{\Gamma f^2 \varrho_0}, \qquad K = \sqrt{\frac{f^2 \varrho_{\mathrm{h}}^2 \kappa_{\mathrm{h}}}{\gamma}}, \tag{10}$$

  where $\kappa_{\mathrm{h}} = (\varrho_0 p'(\varrho_0))^{-1}$ is the isothermal compressibility in the homogeneous state associated to the equation of state $p(\varrho)$. Figure 2 shows the function $\tau^{-1}(k)$ for the three qualitatively different cases: if (i) $\lambda K < 1$ the homogeneous state is stable ($\tau(k) < 0$ for all k), whereas if (ii) $\lambda K > 1$ the amplitude of the long–wavelength perturbations with

  $$k < K_{\mathrm{c}} := K\sqrt{1 - \frac{1}{(\lambda K)^2}} \tag{11}$$

  grows in time. (Case (iii), $\lambda K = \infty$, reflects the gravitational, Newtonian limit of (ii)). This is known as Jeans' instability in a self–gravitating gas but formally the same kind of instability exists in other systems, e.g., in models of cellular chemotaxis [47]. Both Jeans' time and wave number vary in a wide range upon changing the system parameters; as discussed in detail in Ref. [44], the Jeans' instability can be observable in realistic experimental configurations.

Qualitatively the instability is a direct consequence of the fact that the capillary energy per particle scales like λ^2 and can thus be much larger than the energy per particle due to thermal motion and other interactions. In a system of finite size L, the evolution resembles the gravitational instability responsible for cosmological structure formation when $\lambda \gg L$ ("Newtonian limit") because the largest possible modes are unstable and grow the fastest. In the opposite limit, $L \gg \lambda$ (but still $\lambda \gg$ microscopic lengths), the instability resembles spinodal decomposition because the fastest growing structures have a preferred size $\ll L$. The transition between these two scenarios is smooth.

- *Collapse of a disk–shaped homogeneous distribution* [44,46]: a particularly interesting case to highlight this transition is the evolution of a disk–shaped distribution of initial radius L and density ϱ_0 (a "top–hat" profile). For this configuration, Eqs. (5,7) can be solved exactly in the Newtonian limit, $\lambda \to \infty$, when $p = 0$, termed "cold collapse" by analogy with the same problem in cosmology[2]:

$$\varrho(\mathbf{r}, t) = \begin{cases} \dfrac{\varrho_0}{1 - t/\mathcal{T}}, & L < \sqrt{1 - t/\mathcal{T}} \\ 0, & L > \sqrt{1 - t/\mathcal{T}}. \end{cases} \tag{12}$$

Here $\mathcal{T}$ is the Jeans' time, Eq. (10), associated to the initial density of the disk.

The cold collapse can be studied as a function of the ratio L/λ. In the limit $L/\lambda \to 0$ one has the solution (12), which is analog to the "Big Crunch" solution in cosmology: the evolution is dominated by the collective collapse as all the particles reach the center simultaneously in a time $\mathcal{T}$. For small values of the parameter L/λ one can obtain the correction to the "Big Crunch" evolution perturbatively [46]: a singularity at the outer rim of the disk is formed at a time slightly larger than $\mathcal{T}$. In the opposite limit, $L/\lambda \gg 1$, the evolution is dominated by the growth of spatially small density perturbations inside the disk in a spinodal–like scenario, whereby the global collapse of the disk is slowed down to time scales much larger than $\mathcal{T}$. In the transition region, $L/\lambda \sim 1$, the evolution is dominated by the formation of a characteristic shockwave–like structure at the outer rim, the formation of the singularity being counteracted locally by the effect of the pressure term. This shockwave is then transported by the global collapse of the disk in a time scale comparable to the Jeans' time $\mathcal{T}$. Figure 3 provides a qualitative summary of the different regimes as function of the relevant parameters.

3.2 Brownian dynamics simulations

The system described above, colloids in 2D interacting with short–ranged repulsions and the long–ranged capillary monopole force, can be simulated conveniently in order to check the validity of the presented model. Consider a two-dimensional collection of N disklike particles of radius R_0 in a box of size $L \times L$ with periodic boundary conditions. We assume overdamped dynamics for the particles and solve the corresponding Langevin equation:

$$\dot{\mathbf{r}} = \Gamma \mathbf{f} + \mathring{\mathbf{r}}, \tag{13}$$

where $\mathbf{f}$ denotes the total force per particle and $\mathring{\mathbf{r}}$ a random displacement of the particle. This latter noise term is delta–correlated in space and time with a uniform probability distribution. Its width depends on the time step Δt and the diffusion coefficient $D = k_B T \Gamma$ and is given by $w = \sqrt{2D\Delta t}$. The total force acting on each

---

[2] Actually, the solution can be found exactly for any radially symmetric configuration, see Appendix C of Ref. [44].

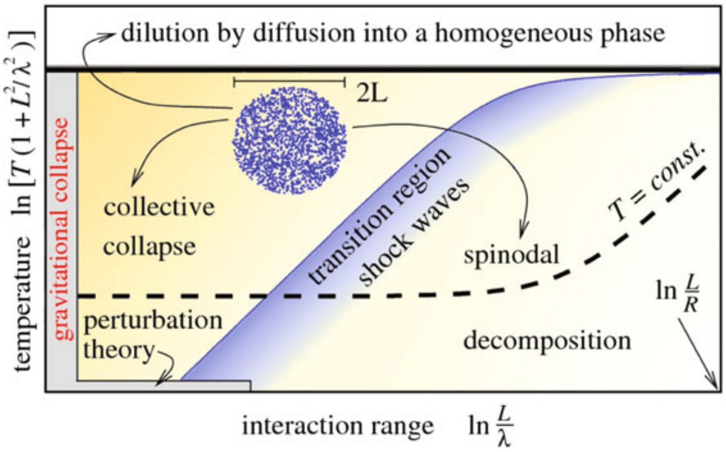

Fig. 3. Qualitative summary of the collapse of a disk–shaped particle distribution in the parameter space (in log–log scale). The horizontal axis represents L/λ (the ratio of the initial radius of the disk and the capillary length), the vertical axis is the ratio of energy of capillary interaction to the other forms of energy of the system (by thermal motion and other, short–ranged interaction forces; the dashed line represents an isotherm in the ideal gas approximation). Adapted from Ref. [46].

particle is given by the sum of short–ranged repulsive forces and the long–ranged capillary force $\mathbf{f} = \mathbf{f}_{\text{cap}} + \mathbf{f}_{\text{short}}$. For the repulsion among the particles we chose the repulsive part of the shifted Lennard–Jones potential, truncated at $d_c/(2R_0) = 2^{1/6}$ and thus mimicking a hard core.

In order to account for the long–ranged nature of the capillary forces in systems with periodic boundary conditions it is necessary to include the periodic images when calculating the force acting on a specific particle. Apart from brute–force methods like summing over as many periodic boxes as needed for a given cut–off parameter λ of the capillary interactions, much faster methods have been developed for simulations in electrostatics and cosmology [48,49,51], both dealing with infinitely ranged potentials. We chose the particle–mesh (PM) method. The basic idea is to solve the equation for the mean–field interfacial deformation (Eq. (5)) by means of discrete Fourier transformation on a grid. Accordingly, Eq. (5) leads to (with Fourier transformed quantities denoted by a tilde):

$$\left(-k^2 - \frac{1}{\lambda^2}\right)\tilde{U} = -\frac{f}{\gamma}\tilde{\varrho}(\mathbf{k}). \tag{14}$$

Denoting the Green's function of the Young–Laplace equation by $\tilde{G}(\mathbf{k}) = -1/(k^2 + 1/\lambda^2)$, and the inverse Fourier transformation by $\mathcal{F}^{-1}$, we can write down the formal solution of Eq. (5) as

$$U(\mathbf{r}) = \mathcal{F}^{-1}\left[-\frac{f}{\gamma}\tilde{G}(\mathbf{k})\tilde{\varrho}(\mathbf{k})\right] \tag{15}$$

and obtain the discretized capillary forces at the grid points according to Eq. (4)

$$\mathbf{f}_{\text{cap}} = f\nabla U(\mathbf{r}) = \mathcal{F}^{-1}\left[\frac{f^2}{\gamma}\imath\mathbf{k}\tilde{G}(\mathbf{k})\tilde{\varrho}(\mathbf{k})\right]. \tag{16}$$

It remains to choose an appropriate discretization scheme in order to map the positions of the particles to the density grid and the grid forces back to the corresponding

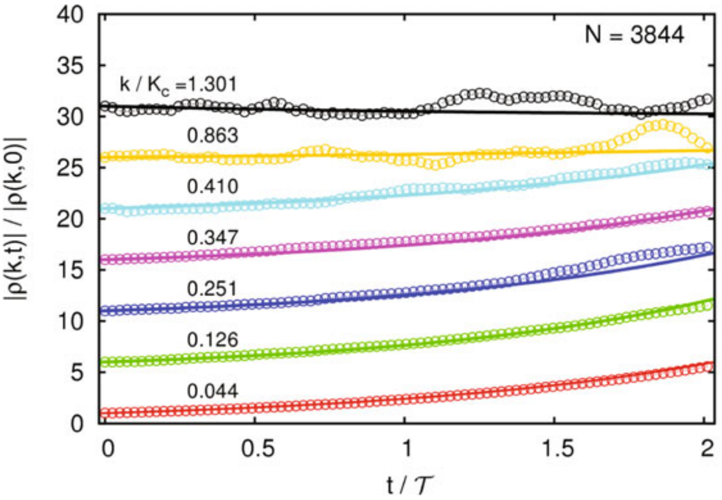

Fig. 4. Evolution of Fourier modes of the initial density distribution $\rho(k,t)$ (normalized by the corresponding value for $t = 0$ and each shifted upwards by 5 for clarity) in a simulation for a $L \times L$ box, $L = 620\,R_0$, with $N = 3844$ particles. The error bars concerning the statistical errors, as obtained from averaging within small time intervals of the order of $\Delta t \approx \mathcal{T}/40$ and over 20 runs of initial configurations, are smaller than the symbol size of the simulation data. The full lines provide the corresponding theoretical prediction for an exponential growth or damping. The figure is taken from Ref. [45], where further details of the simulation can be found. With kind permission of the European Physical Journal (EPJ).

particles. For suitable choices and further details of the implementation, we refer to Ref. [45]. This method guarantees the appropriate incorporation of the long–ranged forces without introducing any additional cutoffs, and accuracy down to the scale of the grid spacing ($r_c = R_0$).

3.2.1 Linear instability of a homogeneous state

We carried out simulations with realistic parameters for microcolloids at a water interface whose weight gives rise to a large enough capillary potential ($N = 3844$, $R_0 = 10\,\mu$m, $L = 6.2\,$mm, $\lambda = 2.7\,$mm, $\gamma = 72\,$mN/m, $V_0 = f^2/(2\pi\gamma) = 0.89\,k_{\rm B}T$, $\Gamma = 10.6 \times 10^{-6}\,$s/kg). In order to check the prediction given by Eq. (9) [45], we compare the evolution of Fourier density modes (normalized with respect to $t = 0$) in Fig. 4. The simulation data agrees nicely with the exponential growth and damping of modes with $k/K < 1$ and $k/K > 1$ respectively. At times $t \gtrsim 1.5\,\mathcal{T}$, deviations become more pronounced. These deviations are attributed to the formation of clusters, as can be inferred from the simulation snapshots presented in Fig. 5. Starting from times $t \gtrsim 1.5\,\mathcal{T}$ a merging of clusters is observed, not captured by the linear stability analysis underlying Eq. (9). This "cluster dynamics" can be addressed with the help of the dynamical quantities n_c, the number of clusters, and the mean cluster size S [45]. We studied the evolution of these quantities for different values of the screening parameter λ/L, in order to investigate the influence of the range of the interaction on the clustering phenomenology. Note that such a tuning of the interaction range is also possible for experimental systems [45]. Inspection of Fig. 6 yields support for a smooth transition between systems with short–ranged, van–der–Waals–like attractions and long–ranged attractive systems resembling a self gravitating system of hard disks. One observes two distinct regimes, both in the temporal evolution and

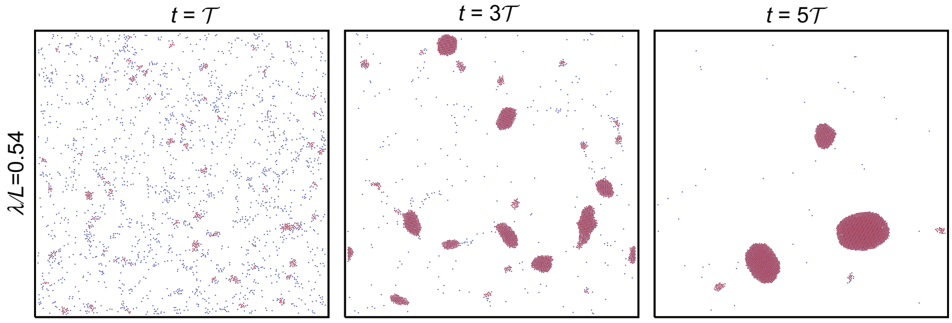

Fig. 5. Snapshots of the particle distribution in $L \times L$ boxes with $L = 500R_0$ at times $\mathcal{T}$, $3\mathcal{T}$, and $5\mathcal{T}$ for a long–ranged capillary attraction with $\lambda/L = 0.54$, corresponding to the usual air–water interface. Clusters (i.e., particles with at least 3 neighbors within a distance of $3.25R_0$) are depicted in red.

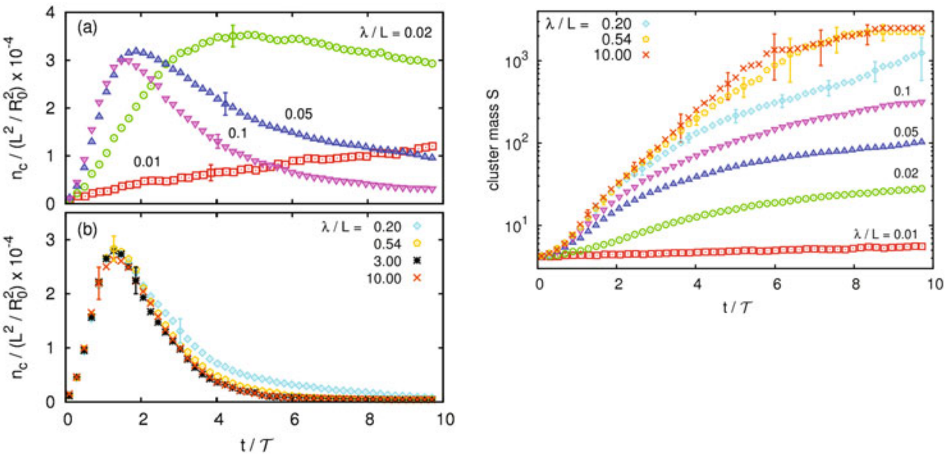

Fig. 6. Evolution of the areal number density n_c/L^2 of clusters (left) and the mean cluster mass $S(t)$ (right) for several values of λ/L, exhibiting the crossover from "short–ranged" attraction (left upper plot (a), $\lambda \lesssim L$) to "long–ranged" attraction (left lower plot (b), $\lambda \gtrsim L$). Only representative error bars are shown, the figures are taken from Ref. [45]. With kind permission of the European Physical Journal (EPJ).

in the dependence on the range parameter: For large λ a rapid clustering occurs up to $t \simeq 1.5\,\mathcal{T}$, manifest in the peak of the number of clusters n_c at that time. Afterwards, in the domain growth stage, n_c decreases as the clusters merge, and ultimatively form one single cluster. The evolution scales for $\lambda/L \geq 0.2$ and becomes independent of the range parameter for larger values. The timescale of the evolution is indeed set by the characteristic time $\mathcal{T}$ as defined in Eq. (10), thus, the overall picture well fits the phenomenology of a self gravitating fluid. For small values of the range parameter, i.e. $\lambda/L \lesssim 0.1$, no scaling is visible and the maximum in the number of clusters depends on λ/L. As there is no characteristic timescale and the cluster mass grows like a power–law (see right panel of Fig. 6), we conclude that spinodal decomposition is the governing mechanism of clustering. Note that these results are independent of the particular choice how a cluster is defined [45].

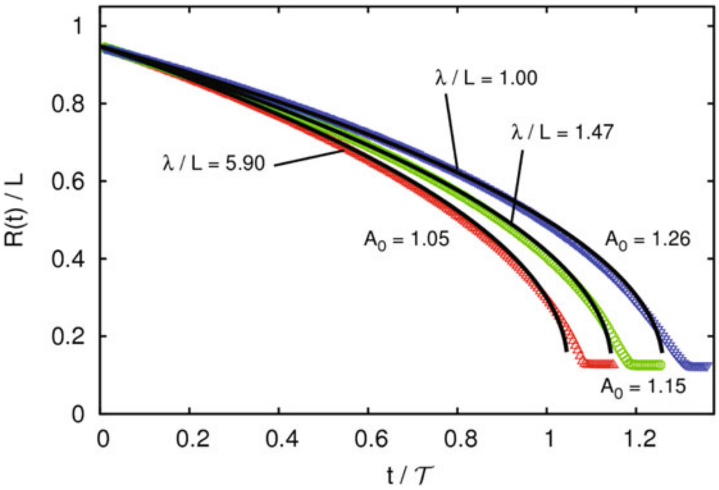

Fig. 7. Evolution of the radius for the outermost ring for $\lambda/L = 1$, 1.48, 5.9 and initial disk radius $L = 183\,R_0$. The full lines correspond to the expression in Eq. (17). As expected from Eq. (12) it turns out that $A_0(\lambda \to \infty) = 1$. (Figure taken from Ref. [45]). With kind permission of the European Physical Journal (EPJ).

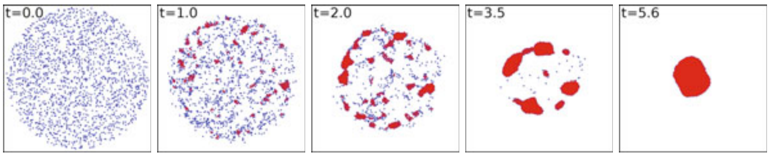

Fig. 8. Snapshots from BD simulations for $\lambda/L = 0.25$. Small clusters predominantly form at the outer rim and collectively move towards the center. (Figure taken from Ref. [46].)

3.2.2 Cold collapse

Furthermore we can test in more detail the evolution of a finite, disklike patch of radius L, in particular the deviations from the cold collapse scenario, as described in the previous section for an infinitely ranged attractive potential. For values of the screening length $\lambda/L \gtrsim 1$ we have monitored the trajectory (time–dependent radius) of circular rings of particles which could be well described by the formula

$$R(t) - R_f = (R_i - R_f)\sqrt{1 - \frac{t}{A_0 \mathcal{T}}}. \tag{17}$$

Here, R_i and R_f denote the initial and final radius of the ring (when the system has reached a close–packed state). The values $R_f = 0$ and $A_0 = 1$ correspond to the cold–collapse limit (see Eq. (12) and Refs. [44,45] for more details). The modified evolution according to Eq. (17) data nicely fits the simulation data. As the capillary length λ is varied (see Fig. 7) the value of the A_0-parameter also changes. If λ/L (the system size L is now given by the radius of the initial patch) increases, A_0 approaches 1, as expected from the cold collapse scenario (infinite range). Thus for the range $\lambda/L > 1$ we find a slowdown of the collapse as λ decreases from infinity but no qualitative change in the collective dynamics.

However, the dynamics is changed qualitatively for $\lambda/L < 1$. Figure 8 depicts several snapshots of a simulation run with $N = 1804$ particles and $\lambda/L = 0.25$. As the system evolves, a ringlike meta–structure of clusters of particles is formed at the

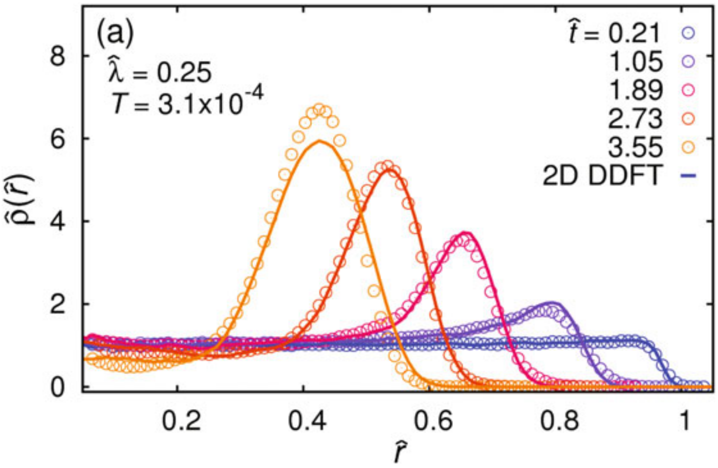

Fig. 9. Evolution of the radial density profile for $T = T_{\text{eff}} = 3.1 \times 10^{-4}$ and $\hat{\lambda} = \lambda/L = 0.25$. The colored lines correspond to the 2D–DDFT numerical results, whereas Brownian dynamics simulation data are indicated by symbols (Figure taken from Ref. [46]).

outer rim of the distribution which slowly travels towards the center. In terms of an azimuthally averaged density profile, this ring corresponds to an inbound traveling density shockwave. For a closer investigation, we introduce dimensionless variables as follows:

$$\hat{r} = \frac{r}{L},\ \hat{\varrho} = \frac{\varrho}{\varrho_0},\ \hat{p} = \frac{p}{k_{\mathrm{B}} T \varrho_0},\ \hat{\lambda} = \frac{\lambda}{L},\ \hat{t} = \frac{t}{\mathcal{T}}, \tag{18}$$

and an effective temperature according to

$$T_{\text{eff}} = \frac{\gamma k_{\mathrm{B}} T}{f^2 \varrho_0 L^2}. \tag{19}$$

Accordingly, the dimensionless mean–field interfacial deformation is $\hat{U} = \varrho_0 L^2 \gamma / f\, U$ and the continuity equation (Eq. (7)) reads [46]

$$\frac{\partial \hat{\varrho}}{\partial \hat{t}} = -\nabla(\hat{\varrho} \nabla \hat{U} - T_{\text{eff}} \nabla \hat{p})\ . \tag{20}$$

It can be viewed as a simple dynamic density functional theory (DDFT) for the collapsing disk. We integrated this equation numerically and compared the result to the Brownian dynamics simulation. For $\lambda/L = 0.25$ and $T_{\text{eff}} = 3.1 \times 10^{-4}$, the result is shown in Fig. 9. The DDFT density profiles nicely agree with the simulation data points for a wide range of times. A pronounced inbound shockwave is visible, confirmed also by analytical perturbation theory of the cold collapse scenario for finite interaction range [46]. The summary of all these findings lead to the proposed "dynamic phase diagram" (Fig. 3): The fate of a disklike patch of particles subject to attractive interactions is determined by the range and the effective temperature of the system. A collective collapse for long–ranged systems is replaced by a shockwave phenomenology for intermediate ranges, whereas spinodal decomposition reigns in the short ranged regime.

As the system of colloidal particles trapped at a fluid interface is at least partially immersed in a fluid phase, the question of the influence of hydrodynamics arises. Within the overdamped limit, hydrodynamic interactions (HI) can be easily added to

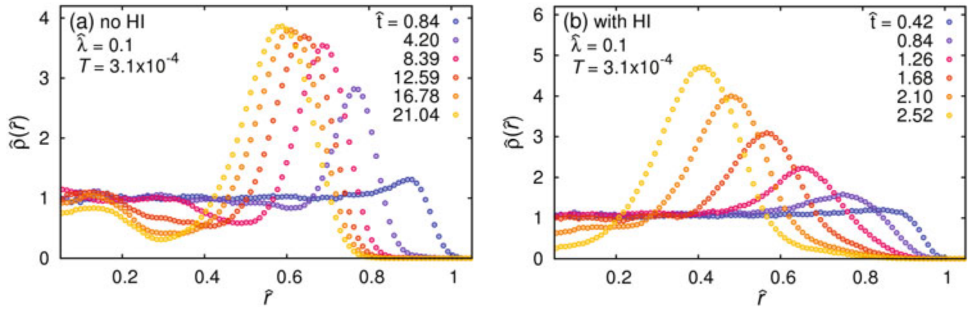

Fig. 10. Left panel: evolution of the radial density profile for $T = T_{\text{eff}} = 3.1 \times 10^{-4}$ and $\hat{\lambda} = \lambda/L = 0.1$ without hydrodynamic interactions. Right panel: the same but with HI included.

Brownian dynamics, leading to (truncated) Stokesian dynamics (tSD) [50,51] simulations. The term truncated refers to the fact that the series expansion for the hydrodynamic interaction tensor, or mobility matrix is truncated at the Rotne–Prager level, capturing the far–field of the hydrodynamic interactions on the two–body level only. As a test case in order to check the influence of HI on our system of colloids, we chose a setup with a pronounced, slowly inbound moving shockwave, i.e. $\hat{\lambda} = \lambda/L = 0.1$ and $T_{\text{eff}} = 3.1 \times 10^{-4}$. In Fig. 10 we compare the evolution of the system with (right panel) and without hydrodynamic interactions (left panel). The phenomenology remains unchanged, however, a significant change of the corresponding timescale is observed. Including HI, the evolution speeds up and the corresponding timescales differ roughly by one order of magnitude.

4 Conclusion and outlook

In this article, we reviewed two aspects of the physics associated with colloids trapped at fluid interfaces. Both aspects confirm the usefulness of colloidal systems as model systems also for the interface case. First, it was shown that the far–field electrostatic interactions between charged colloids at an interface are proportional to the surface potential which in turn sensitively depends on the properties of the electrostatic double layer near the colloids. Here, we examined the capability of several modifications to the Poisson–Boltzmann equation to describe existing experimental data for the far–field interaction. For the future, it would be worthwhile to measure these interactions also for different counterions to establish ion–specific effects on the surface potential and to aid further model building aiming to include these ion–specific effects. – Second, colloids at an interface can be used to create a model system with long–ranged, logarithmic capillary attractions (as in 2D Newtonian gravity), cut off at the capillary length. The dynamics in such a system is dominated by collective effects and can be captured by an appropriate mean–field model. The long–ranged attractions lead to an instability of the system towards a collapsed state. The capillary length is hereby a control parameter which allows to continuously switch from the collective dynamics associated with unbound attractions to spinodal decomposition as seen in systems with short–ranged attractions. In the transition region between these two scenarios, novel phenomena may be found as the example of the travelling shock wave for the collapsing disk has shown. It would be very desirable to perform experiments with colloids of about 10 μm size to investigate these dynamic regimes. Another future prospect is derived from the simulation result that additional far–field hydrodynamic interactions speed up the collective dynamics compared to just

Brownian dynamics. Ongoing work shows that this is a phenomenon linked to the confinement of colloids to 2D but with hydrodynamic interactions acting through a 3D solvent [52] and has far–reaching consequences for the colllective diffusion coefficient in such systems. This appears to be another fruitful route to explore the physics of partially confined systems.

This work was supported by the DFG within SFB TR6 (Junior Research Group N1 "Colloids at interfaces").

References

1. B.J. Park, J.P. Pantina, E.M. Furst, M. Oettel, S. Reynaert, J. Vermant, Langmuir **24**, 1686 (2008)
2. K. Masschaele, B.J. Park, E.M. Furst, J. Fransaer, J. Vermant, Phys. Rev. Lett. **105**, 048303 (2010)
3. B.J. Park, J. Vermant, E.M. Furst, Soft Matter **6**, 5237 (2010)
4. A.D. Law, D.M.A. Buzza, T.S. Horozov, Phys. Rev. Lett. **106**, 128302 (2011)
5. A.D. Law, M. Auriol, D. Smith, T.S. Horozov, D.M.A. Buzza, Phys. Rev. Lett. **110**, 138301 (2013)
6. P.A. Kralchevsky, K. Nagayama, Adv. Colloid Interface Sci. **85**, 145 (2000)
7. F. Bresme, M. Oettel, J. Phys.: Condens. Matter **19**, 413101 (2007)
8. M. Oettel, S. Dietrich, Langmuir **24**, 1425 (2008)
9. A. Domínguez, *Capillary Forces between Colloidal Particles at Fluid Interfaces*, in *Structure and Functional Properties of Colloidal Systems*, edited by R. Hidalgo-Alvarez (CRC Press, Boca Raton, FL, 2010), p. 31
10. D. Frydel, A. Domínguez, M. Oettel, Phys. Rev. E(R) **77**, 020401 (2008)
11. D. Frydel, S. Dietrich, M. Oettel, Phys. Rev. Lett. **99**, 118302 (2007)
12. A. Shrestha, K. Bohinc, S. May, Langmuir **28**, 14301 (2012)
13. I. Borukhov, D. Andelman, H. Orland, Phys. Rev. Lett. **79**, 435 (1997)
14. A. Abrashkin, D. Andelman, H. Orland, Phys. Rev. Lett. **99**, 077801 (2007)
15. D. Frydel, M. Oettel, Phys. Chem. Chem. Phys. **13**, 4109 (2011)
16. D. Frydel, J. Chem. Phys. **134**, 234704 (2011)
17. M.M. Hatlo, R. van Roij, L. Lue, EPL **97**, 28010 (2012)
18. I. Kalcher, J.C.F. Schulz, J. Dzubiella, Phys. Rev. Lett. **104**, 097802 (2010)
19. D. Frydel, Y. Levin, J. Chem. Phys. **137**, 164703 (2012)
20. K.D. Danov, P.A. Kralchevsky, J. Coll. Interface Science **345**, 505 (2010)
21. K.D. Danov, P.A. Kralchevsky, Adv. Coll. Interface Science **154**, 91 (2010)
22. A. Domínguez, M. Oettel, S. Dietrich, J. Chem. Phys. **128**, 114904 (2008)
23. N. Aubry, P. Singh, Phys. Rev. E **77**, 056302 (2008)
24. N. Aubry, P. Singh, M. Janjua, S. Nudurupati, Proc. Nat. Acad. Sciences USA **105**, 3711 (2008)
25. K. Masschaele, J. Vermant, Soft Matter **7**, 10597 (2011)
26. B. Madivala, J. Fransaer, J. Vermant, Langmuir **25**, 2718 (2009)
27. J.C. Loudet, B. Pouligny, EPL **85**, 28003 (2009)
28. J.C. Loudet, B. Pouligny, Eur. Phys. J. E **34**, 76 (2011)
29. E.P. Lewandowski, M. Cavallaro, Jr., L. Botto, J.C. Bernate, V. Garbin, K.J. Stebe, Langmuir **26**, 15142 (2010)
30. M. Cavallaro Jr., L. Botto, E.P. Lewandowski, M. Wang, K.J. Stebe, Proc. Nat. Acad. Sciences USA **108**, 20923 (2011)
31. L. Botto, L. Yao, R.L. Leheny, K.J. Stebe, Soft Matter **8**, 4971 (2012)
32. L. Botto, E.P. Lewandowski, M. Cavallaro Jr., K.J. Stebe, Soft Matter **8**, 9957 (2012)
33. M. Oettel, A. Domínguez, M. Tasinkevych, S. Dietrich, Eur. Phys. J. E **28**, 99 (2009)
34. L. Yao, L. Botto, M. Cavallaro Jr., B.J. Bleier, V. Garbin, K.J. Stebe, Soft Matter **9**, 779 (2013)

35. J. Guzowski, M. Tasinkevych, S. Dietrich, Eur. Phys. J. E **33**, 219 (2010)
36. J. Guzowski, M. Tasinkevych, S. Dietrich, Phys. Rev. E **84**, 031401 (2011)
37. J. Guzowski, M. Tasinkevych, S. Dietrich, Soft Matter **7**, 4189 (2011)
38. A. Würger, Phys. Rev. E **74**, 041402 (2006)
39. D. Ershov, J. Sprakel, J. Appel, M.A. Cohen Stuart, J. van der Guch, Proc. Nat. Acad. Sciences USA **110**, 9220 (2013)
40. A. Vincze, A. Agod, J. Kertész, M. Zrínyi, Z. Hórvölgyi, J. Chem. Phys. **114**, 520 (2001)
41. P. Singh, D.D. Joseph, S.K. Gurupathama, B. Dalala, S. Nudurupatia, Proc. Nat. Acad. Sciences USA **106**, 19761 (2009)
42. J. de Graaf, M. Dijkstra, R. van Roij, J. Chem. Phys. **132**, 164902 (2010)
43. N. Chatterjee, S. Lapin, M. Flury, Environ. Sci. Technol. **46**, 4411 (2012)
44. A. Domínguez, M. Oettel, S. Dietrich, Phys. Rev. E **82**, 011402 (2010)
45. J. Bleibel, A. Domínguez, M. Oettel, S. Dietrich, Eur. Phys. J. E **34**, 125 (2011)
46. J. Bleibel, S. Dietrich, A. Domínguez, M. Oettel, Phys. Rev. Lett. **107**, 128302 (2011)
47. P.-H. Chavanis, C. Sire, Physica A **387**, 4033 (2008)
48. R.W. Hockney, J.W. Eastwood, *Computer Simulation Using Particles* (Hilger, Bristol, 1988)
49. M. Deserno, C. Holm, J. Chem. Phys. **109**, 7678 (1998)
50. J.F. Brady, G. Bossis, Ann. Rev. Fluid Mech. **20**, 111 (1988)
51. J. Bleibel, J. Phys. A: Math. Theor. **45**, 225002 (2012)
52. J. Bleibel, A. Domínguez, F. Günther, J. Harting, M. Oettel, *Hydrodynamic interactions induce anomalous diffusion under partial confinement* [`arXiv:1305.3715`] (2013)